RSC Advances

ROYAL SOCIETY OF CHEMISTRY

PAPER

View Article Online
View Journal | View Issue

Check for updates

Cite this: *RSC Adv.*, 2026, **16**, 21925

Enhanced Photodetectivity and responsivity of Bi-S films for visible light photodetectors: an experimental and density functional theory study

L. Mahapatra,[a] D. Kar,[ab] B. Mohanty,[b] Prabhukrupa C. Kumar,[b] D. Alagarasan,[c] C. Sripan,[d] R. Swain,[e] J. Kumar,[ef] S. Brahma[g] and R. Naik*[b]

Received 27th February 2026
Accepted 14th April 2026

DOI: 10.1039/d6ra01732k

rsc.li/rsc-advances

Thermal annealing provides a facile method for tuning the optoelectronic response of semiconductor thin films. In this work, ~700 nm-thick Bi_2S_3 thin films prepared by thermal evaporation were subjected to annealing in the range of 100–200 °C, and their structural, optical and photodetection properties were studied. Annealing brings about changes in the crystallinity, surface morphology, and wettability, resulting in a decrease in the bandgap from 1.022 to 0.766 eV with increasing temperature. Crystallinity improves at moderate annealing temperatures (100–150 °C) but worsens at higher temperatures (200 °C) because the lattice becomes more disordered. The refractive index and nonlinear optical parameters, such as nonlinear refractive index and nonlinear absorption coefficient, are found to increase with an increase in the annealing temperature. Photodetector response studies reveal an increase in the responsivity from 0.129 to 0.822 A W^{-1} and an increase in the specific detectivity from 5.17×10^9 to 1.34×10^{10} Jones with increasing annealing temperature. The results of density functional theory (DFT) calculations are also presented, which support the experimental results. It is conclusively shown that annealed Bi_2S_3 thin films can be employed as sensitive visible-light photodetectors.

1. Introduction

Among the various compounds of chalcogenides, metal chalcogenide-based semiconductors are promising candidates for numerous useful applications. These include strong-absorption solar cells, photovoltaics, electrodes for photoelectrochemical reactions for fuel generation, photodetectors, supercapacitors, and other components.[1–5] Among such materials, Bi_2S_3 has gained considerable attention due to its suitable properties. It is basically an n-type V-VI semiconductor with a direct bandgap energy of 1.3–1.7 eV.[6] Bi_2S_3 is a non-hazardous, inexpensive material due to its great natural abundance and high absorption coefficient ($\sim 10^5$ cm^{-1}). It also has a high carrier mobility ($\mu e = \sim 200$ cm^2 V^{-1} s^{-1}), which is suitable for complete light absorption and efficient photogenerated carrier collection at a high thickness.[7] The important applications of Bi_2S_3 include thermoelectric devices, photodiodes, infrared detectors, hydrogen sensors, and photovoltaics.[8–11] Using low-cost Bi_2S_3 thermoelectric materials, it is possible to fabricate an environmentally friendly and cost-effective high-performance thermoelectric hydrogen sensor.[11] Bi_2S_3 films in a nanocrystalline form have potential applications in photoelectrochemical (PEC) water splitting.[12] Bi_2S_3 films act as potential electrodes with a specific capacitance of 289 F g^{-1} in a supercapacitor.[13] The Bi_2S_3 film photodetector deposited at 350 °C is good for commercial optoelectronic applications. This photodetector exhibits a responsivity of 1.58×10^{-1} A W^{-1} and a detectivity of 9.75×10^9 Jones. Its external quantum efficiency (EQE) is 50.8% with response/decay times of 0.3/0.4 s, respectively.[14] The Bi_2S_3 film prepared on a fluorophlogopite mica substrate through chemical vapour deposition possesses a response range from 365 to 940 nm. The long-term stability of the Bi_2S_3 photodetector has also been verified by storing it for 6 months in air and then measuring its instantaneous on/off behaviour over 500 cycles.[15] The Bi_2S_3 film prepared by the chemical deposition method exhibits variations in optical properties with the thickness. The 50 nm-thick film exhibits a V_{oc} of 440 mV and a J_{sc} of 0.022 mA cm^{-2}.[16] The pulsed laser-deposited Bi_2S_3 films exhibit n-type conductivity at room temperature. The film prepared at a substrate temperature between 150 °C and 200 °C exhibits very good characteristics for optoelectronic applications.[17] The Bi_2S_3 thin films synthesized through an economical and simply modified SILAR method

---

[a] *Department of Physics, Nayagarh Autonomous College, Nayagarh, 752069, India*

[b] *Department of Engineering and Material Physics, ICT-IOC, Bhubaneswar, 751013, India. E-mail: ramakanta.naik@gmail.com*

[c] *Department of Physics, Nitte Meenakshi Institute of Technology (NMIT), Nitte (Deemed to be University), Bengaluru, 560064, India*

[d] *Department of Physics, Dayananda Sagar Academy of Technology and Management, Udayapura, Bangalore, 560082, India*

[e] *Department of Physics, Utkal University, Bhubaneswar 751004, India*

[f] *Department of Physics and Astrophysics, University of Delhi, Delhi-110007, India*

[g] *Department of Physics, Madanapalle Institute of Technology and Science, Deemed to be University, Madanapalle, Andhra Pradesh, 517325, India*

demonstrate an improvement in crystallinity and a high absorption strength in the visible range.[18]

The different applications of Bi_2S_3 rely on the kind of deposition or preparation method used. These can be achieved through various physical and chemical synthesis processes, including hydrothermal,[19] SILAR,[18] spray pyrolysis,[20] solvothermal,[21] electro-deposition,[22] thermal evaporation,[23] chemical vapour deposition,[24] dip coating,[25] and chemical bath deposition.[26] For large-scale production with industrial and low-cost requirements, thermal evaporation is a cost-effective, simple, and scalable method. Further improvements are required in the optical, structural, electrical and other properties of thin films. For this purpose, various post-synthesis treatments have been employed, including heavy ion irradiation, thermal annealing, laser irradiation, gamma-ray irradiation, and proton irradiation.[27–31] Among the various methods, thermal annealing is a very simple, low-cost, and environmentally friendly way to modify the layer properties of the films. Annealing depends on the heat treatment duration, the amount of heat, annealing conditions, and other factors.[32] In general, the postdeposition annealing of a film through heat treatment induces structural relaxation, leading to the equilibrium state in the film and variations in its electrical and optical behaviour. This is because the unannealed film has a very high relaxation time at room temperature.[33] The variables, such as the annealing duration and annealing temperature, affect the stress in the film, along with the defects and the dopant atoms present. This influences the carrier dynamics and bandgap of the film.[34] The crystallinity increases with heat treatment, resulting in improvements in transport and optical behaviour as well as surface modification, which is favourable for many applications. The Bi_2S_3 films prepared by the chemical bath deposition method exhibit improved crystallinity and increased conductivity upon annealing.[26] A report is available on the improved performance of Bi_2S_3 films deposited at increased substrate temperatures.[14]

However, there is no report on the annealing temperature-dependent modification of Bi_2S_3 films prepared by thermal evaporation. The present study focuses on the behavior of thermally evaporated Bi_2S_3 films under different annealing temperatures, such as 100 °C, 150 °C, and 200 °C. While thermal evaporation is a scalable and cost-effective technique, systematic investigations of annealing temperature effects on such films are largely missing. Most reports focus on isolated properties (*e.g.*, only optical or structural), and a unified study linking structural, wettability, optical, nonlinear, and photodetection properties is lacking. Previous works do not sufficiently explain bandgap modulation and defect-induced changes through controlled annealing. There is a lack of combined experimental and theoretical validation using density functional theory (DFT) to explain the electronic and optical behavior of the material. This work is novel because it systematically studies how annealing changes multiple properties of thermally evaporated Bi_2S_3 thin films. This is done through a combination of experiments and DFT analysis, which greatly improves the performance of photodetectors.

The prepared Bi_2S_3 films were annealed at different temperatures and characterised using various experimental techniques to observe the changes in the film after annealing compared to the unannealed state. The optical (linear and nonlinear) behaviour was probed through UV-visible spectroscopy, while the surface wettability was investigated through contact angle analysis. Morphological changes were observed using FESEM, and structural changes were detected by XRD. The electrical conductivity was measured using a Keithley 2450 source meter.

2. Details of the experimental process

2.1. Thin film deposition

Bi_2S_3 films of ∼700 nm thickness were deposited from high-purity (99.999%) Bi_2S_3 ingots purchased from Sigma-Aldrich. The Bi_2S_3 thin films were synthesized using a physical vapor deposition method, specifically *via* a thermal evaporation process with a Smart Coat 3 HHV instrument. Before deposition, the glass substrates were cleaned with a standard method that included washing with detergent, rinsing with deionized water, and drying. The deposition took place at room temperature, and a steady, high vacuum (about 10^{-5} Torr) was maintained the whole time. The normal room temperature was maintained inside the chamber during deposition by circulating water through the chiller. The film coating was deposited at a 5 Å s^{-1} rate. To achieve uniformity in thickness, the substrate was continuously rotated by a small-speed motor. The film thickness was monitored using a thickness monitor attached to the coating unit. The prepared films were cut into pieces for annealing purposes. The films were thermally annealed at various temperatures, including 100 °C, 150 °C, and 200 °C, for 2 hours. The annealing process was carried out in ambient air using a conventional furnace without a controlled atmosphere. The schematic of annealing is shown in Scheme 1.

2.2. Characterisation of the films

The annealed and as-deposited Bi_2S_3 films were characterised by various techniques to understand their behaviour. The structure of the films was obtained from XRD data analysis. The XRD data were recorded using the D8 Advance Bruker instrument with a CuK_α source with $\lambda = 0.1541$ nm. The data in the 2θ range from 10° to 60° were recorded at a 0.03° sec^{-1} step size with a glancing angle of 1°. Further structural information was collected from HRTEM. The TEM and SAED images at various magnifications were obtained using the JEOL HRTEM unit. The film thickness was further double-checked through cross-section FESEM images. The presence of the elements in the film was studied by EDX. The change in the film's surface morphology after annealing was observed by an FESEM instrument (JEOL-JSM-7610F). The wettability behaviour was measured by a contact angle meter (DMe-211 Plus make). A 0.5 μL deionized water drop was employed to collect the data at 2–3 positions to minimize the error. The transmission spectra were recorded using a UV-visible spectrophotometer (JASCO V-770) within the 500–2500 nm wavelength range. The resolution of

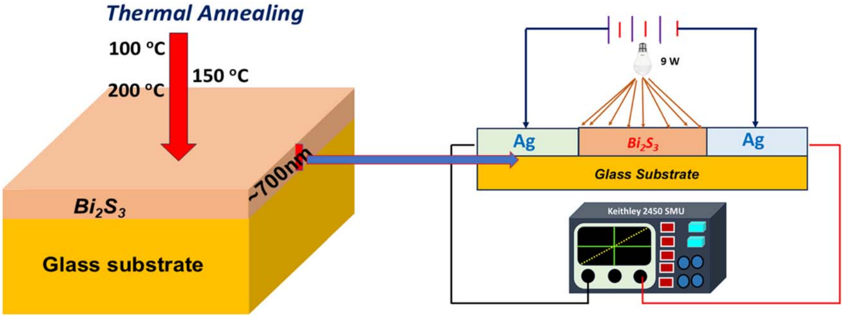

Scheme 1 Schematics of the annealing process and *I*–*V* measurement set-up.

the spectrometer was 0.5 nm. A Kratos Analytical Axis Ultra spectrometer was used to obtain the XPS core-level spectra of the 200 °C annealed film. The AlKα X-ray source (1486.6 eV), operating in an ultrahigh vacuum of approximately 2×10^{-9} Torr, was used for the observations. The current–voltage variation was probed by a Keithley 2450 source meter. The applied voltage was from −10 V to +10 V. A 9 W white LED bulb was used to obtain the photocurrent data. The dark and light currents with a step size of 0.03 V were measured. The dark current was initially measured, followed by the measurement of the light current. Scheme 1 illustrates the I-V measurement setup.

3. Results with discussion

3.1. XRD, FESEM, and TEM

The XRD patterns of Bi$_2$S$_3$ films are illustrated in Fig. 1(a). The XRD peaks match well with the standard bismuthinite phase (ICSD code: 00-002-0391). The samples exhibit characteristic reflections corresponding to the (200), (101), (220), (021), (411), and (321) planes corresponding to 2θ values of approximately 15.69°, 23.07°, 23.11°, 27.23°, 38.03°, and 39.93°, respectively, confirming the formation of a polycrystalline structure.

Annealing leads to two primary changes in the diffraction patterns: (i) peak intensity and (ii) peak full-width half-maximum (FWHM). The as-deposited film shows four prominent peaks at different planes, as indexed in Fig. 1(a). The diffraction peaks of the film annealed at 100 °C are more intense and sharper than those of the as-deposited film. This enhancement indicates improved crystallinity, increased long-range atomic ordering, and a reduction in structural defects.[35,36] After annealing at a temperature of 150 °C, there is a gradual decrease in these parameters due to the broadening of the peak width.

The FWHM values show a decrease for 100 °C and 150 °C annealed film as compared to the as-deposited film, signifying grain growth, a reduction in microstrain, and the relaxation of internal stresses. Finally, for the 200 °C annealed film, the peak intensity decreases slightly for some planes and certain peaks broaden again, suggesting disturbed structural ordering at higher temperatures.

The calculated parameters (crystallite size, lattice strain, dislocation density, and crystallite number density) highlight the strong influence of thermal energy on the crystallisation behaviour, which is summarised in Table 1. The crystallite size and lattice strain were estimated using the Debye–Scherrer equation provided below.[36,37] The Debye–Scherrer equation was used to determine the size of the crystallites, but it did not consider the broadening of the instruments. As a result, the values are only rough estimates. However, because all the measurements were taken under the same conditions, the trends we observed are still useful for comparison.

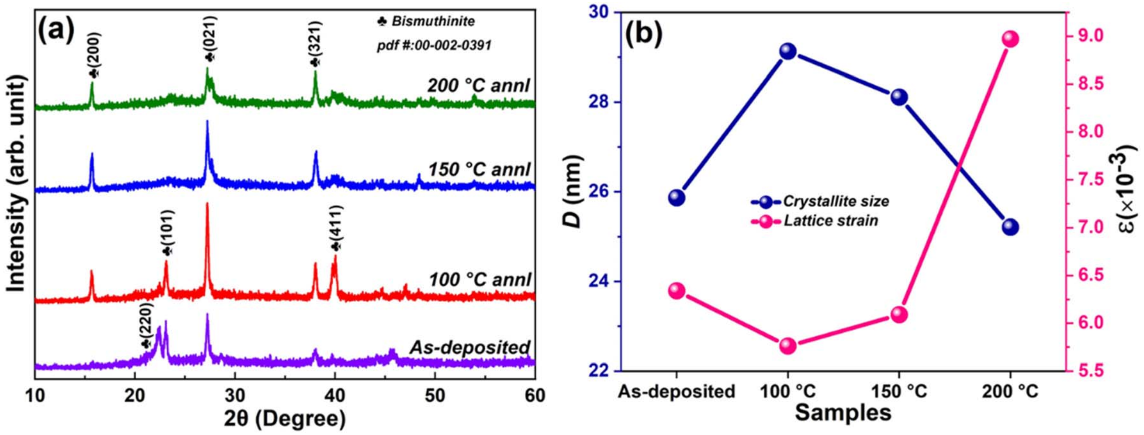

Fig. 1 (a) XRD spectra and (b) comparison of *D* and ε of the samples annealed at 100 °C, 150 °C, and 200 °C.

Table 1 Computed structural data of Bi_2S_3 thin films

Samples	Peak position (degree)	FWHM (degree)	Crystallite size (D) (nm)	Average crystallite size (C) (nm)	Lattice strain (ε) ($\times 10^{-3}$)	Dislocation density (δ) ($\times 10^{-3}$) (nm^{-2})	Crystallites per unit volume (N_c) ($\times 10^{-3}$) (nm^{-2})
Asp	22.37	0.425	19.89	25.86	6.34	1.49	46.25
	23.07	0.304	27.85				
	27.24	0.2677	31.87				
	38.007	0.3683	23.82				
100 °C	15.69	0.2466	33.95	29.13	5.76	1.18	32.36
	23.11	0.2896	29.23				
	27.23	0.2371	35.99				
	38.03	0.2805	31.27				
	39.93	0.5807	15.19				
150 °C	15.69	0.2532	33.06	28.11	6.09	1.26	36.02
	27.26	0.2992	28.52				
	38.07	0.3857	22.75				
200 °C	15.69	0.2183	38.35	25.21	8.97	1.57	49.93
	27.44	0.8958	9.53				
	38.05	0.3162	27.74				

$$C = \frac{0.9\lambda}{\beta\cos\theta} \tag{1a}$$

$$\varepsilon = \frac{\beta}{4\tan\theta} \tag{1b}$$

The XRD pattern was used to calculate the Bragg angle, θ, and the FWHM, β, which are listed in Table 1. In this case, λ is equal to 1.54 Å (the wavelength of CuKα). The as-prepared film shows an average crystallite size of ~25.86 nm. After annealing at 100 °C and 150 °C, the crystallite size slightly increases to 29.13 nm and 28.11 nm, respectively. This suggests that thermal energy facilitates grain growth by reducing microstrain and promoting the coalescence of smaller crystallites.[4] After annealing at 200 °C, the average crystallite size decreases to ~25.21 nm, primarily due to the broadening of the peak at 27.44°, which may arise from agglomeration, local strain accumulation, or the re-nucleation of smaller crystallites at higher temperatures. The observed structural degradation at 200 °C is corroborated by increased peak broadening, elevated lattice strain, and an increased dislocation density, suggesting that excessive thermal energy causes lattice distortion, defect formation, and the potential renucleation of smaller crystallites. Chalcogenide thin films have been reported to exhibit this kind of nonmonotonic annealing behavior, where moderate annealing makes the crystals better, but higher temperatures make the structure less stable.

The microstrain decreases from 6.34×10^{-3} (the as-deposited film) to 5.76×10^{-3} (the 100 °C annealed film), indicating effective thermal relaxation. At this stage, annealing enables trapped defects, dangling bonds, and microstresses to reorganise or annihilate, resulting in a more uniform crystal lattice. After annealing at 150 °C, the strain slightly increases (6.09×10^{-3}), suggesting interactions between grain growth and residual stress redistribution. After annealing at 200 °C, the strain rises sharply to 8.97×10^{-3}, showing that excessive thermal energy introduces new lattice distortions, possibly due to rapid atomic vibration or lattice mismatch during renucleation.[38] Fig. 1(b) presents the variation of D and ε with the annealing temperature.

Dislocation density is defined as the total length of dislocation lines per volume, and it is a key indicator of the defect concentration within a crystal. These dislocations, which arise from lattice irregularities or mismatches, typically originate due to the strain or imperfections introduced during film growth or material synthesis.[39] The dislocation density (δ) was determined using eqn (1c).

$$\delta = \frac{1}{C^2} \tag{1c}$$

It follows the inverse trend of the crystallite size, *i.e.*, the minimum δ is observed at 100 °C (1.18×10^{-3} nm^{-2}), where the crystallite size is the largest, and the maximum δ is observed at 200 °C (1.57×10^{-3} nm^{-2}), reflecting a reduced crystallite size and increased disorder. This confirms that annealing improves the crystal quality up to 100–150 °C, while higher temperatures introduce imperfections. The crystallite number density (N_c) was deduced from eqn (1d).[35]

$$N_c = \frac{d}{C^3} \tag{1d}$$

Here, d is the film thickness, which is 700 nm. It is found that N_c increases systematically with the annealing temperature. The decrease at 100–150 °C corresponds to grain growth (larger crystallites), while the sharp increase at 200 °C indicates the formation of smaller crystallites or renucleation, consistent with increased strain.

The XRD study reveals that controlled annealing has a significant influence on the structure of the films. Annealing at temperatures up to 100–150 °C enhances crystallinity by increasing the crystallite size, reducing the dislocation density, and decreasing macrostrain. However, annealing at 200 °C leads to structural degradation, as evidenced by increased

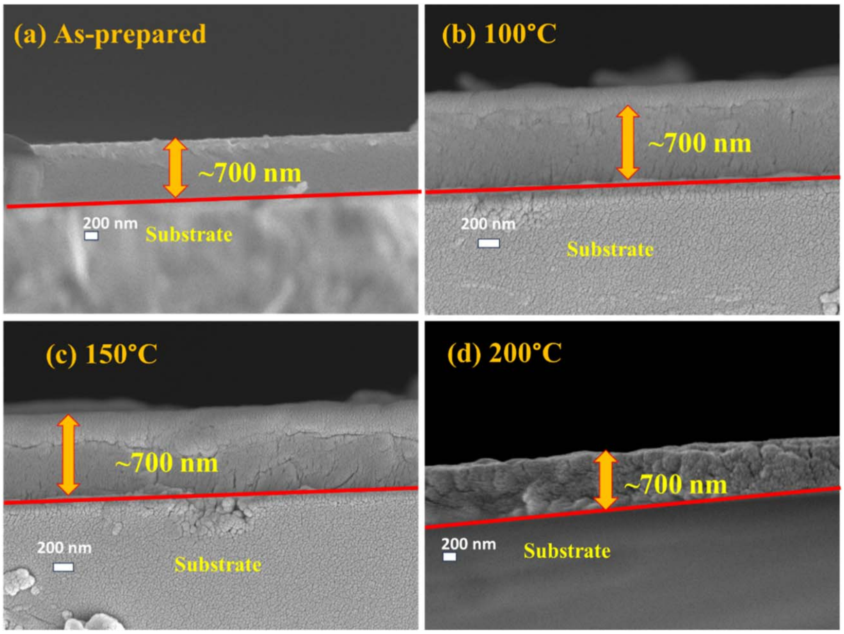

Fig. 2 Cross-section images of the (a) as-deposited, (b) 100 °C annealed, (c) 150 °C annealed, and (d) 200 °C annealed films.

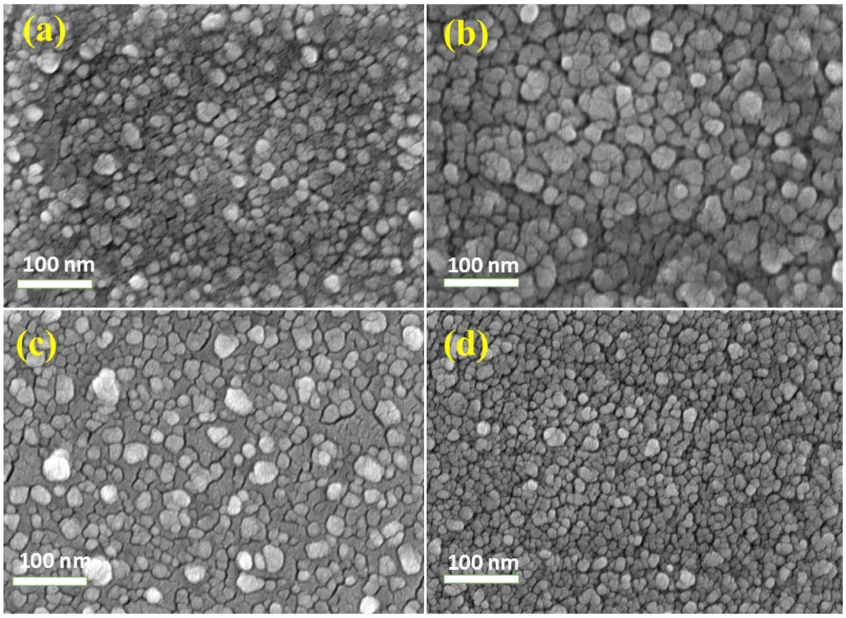

Fig. 3 FESEM images of the (a) as-deposited, (b) 100 °C annealed, (c) 150 °C annealed, and (d) 200 °C annealed Bi_2S_3 films.

strain, a higher dislocation density, and a reduction in the crystallite size.

The cross-sectional view of the as-prepared Bi_2S_3 film indicates a thickness of ~700 nm (Fig. 2(a)). This thickness is further verified and is consistent with the value measured during the deposition process using the thickness monitor. Additionally, there is no change in the thickness upon annealing, as shown in Fig. 2(b–d). However, annealing induces a change in the morphology, which can be clearly seen by comparing the images in Fig. 2(a–d).

The surface morphological changes with annealing are visible in FESEM images, as presented in Fig. 3. The unannealed film's morphology is shown in Fig. 3(a), which clearly indicates a uniform particle distribution over the surface. The particle size increases with increasing annealing temperature up to 100 °C (Fig. 3(b)) and then decreases with a further increase in the temperature, as illustrated in Fig. 3(c and d). This observation is well supported by its average crystallite size evaluated from XRD.

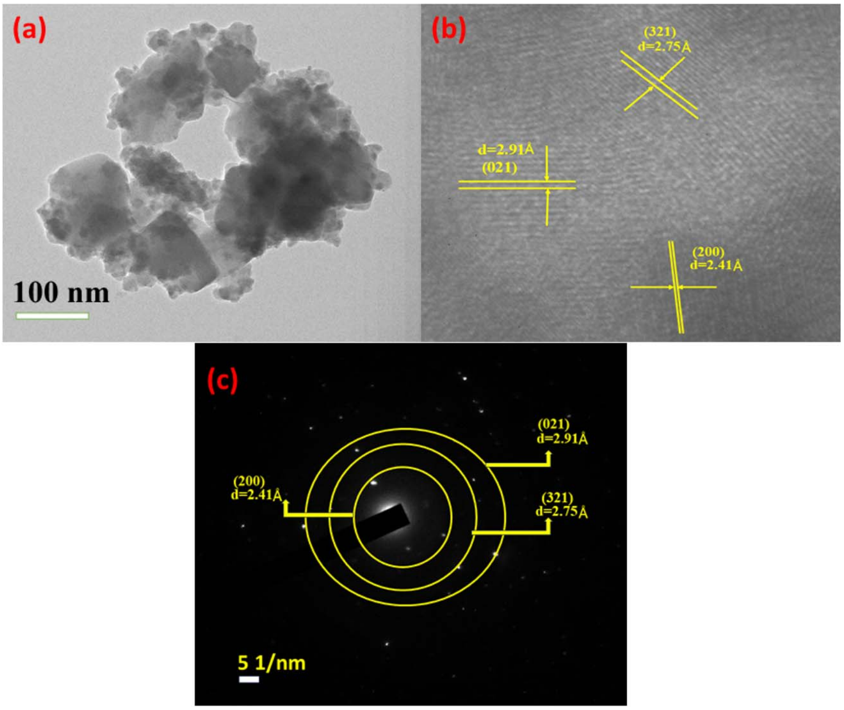

Fig. 4 (a) TEM image at 100 nm magnification, (b) HRTEM fringe pattern and (c) SAED pattern of the 200 °C annealed film.

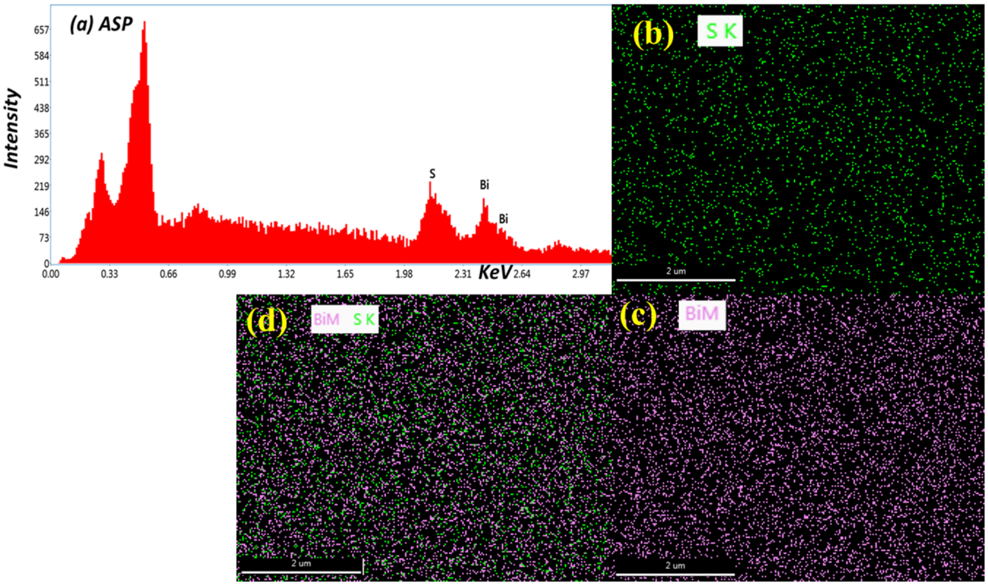

Fig. 5 EDX image for the (a) as-deposited film. Element distribution of (b) S, (c) Bi, and (d) Bi-S in the Bi_2S_3 film.

The TEM image at a 100 nm scale implies the particulate nature of the film morphology. Fig. 4(a) reveals well-dispersed nanostructures with a uniform morphology. The HRTEM analysis presented in Fig. 4(b) provides deep insights into the structure of the material with the presence of different planes. The planes are illustrated by the distinct lattice fringes with interplanar distances, *d*. The (021) plane with $d = 2.91$ Å, the plane (321) with $d = 2.75$ Å, and the plane (200) with $d = 2.41$ Å are well matched with the SAED pattern, as shown in Fig. 4(c). It presents a series of distinct circular rings (diffraction), which imply the polycrystallinity of the films. The diffraction features are in close agreement with the XRD results, thereby validating the presence of multiple crystalline phases.

3.1.1. Composition study by EDX and XPS analyses. Fig. 5(a) shows the EDX spectra of the Bi_2S_3 film in its as-prepared condition, which illustrates the presence of Bi and S with peaks at specific energy levels. The other peaks are due to carbon (C) and gold. The low-intense peak near 0.277 keV is

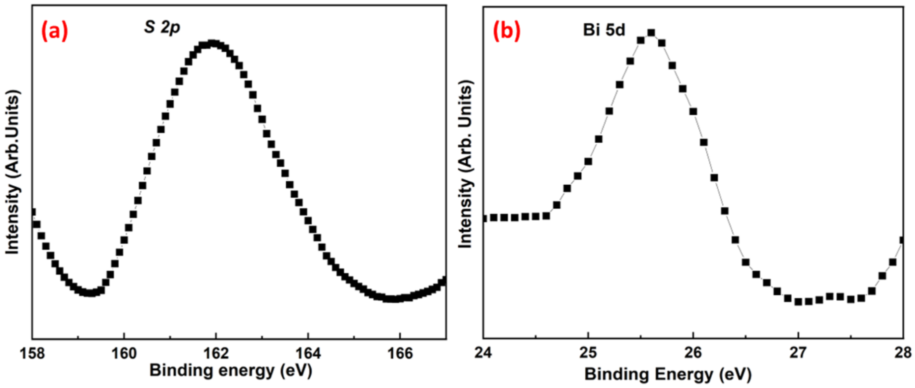

Fig. 6 (a) S 2p (b) Bi 5d core-level XPS spectra of the 200 °C annealed film.

attributed to carbon, which arises from the carbon coating applied for charge neutralisation during imaging. The peak located around 0.51 keV is the characteristic X-ray emission line of gold (Au). The uniform distribution of S and Bi in the as-prepared film is presented by elemental mapping, as shown in Fig. 5(b and c), respectively. The combined elemental distribution in the film is illustrated in Fig. 5(d).

Further verification of the film's elemental composition was conducted using XPS, which is a surface analytical technique for investigating the surface properties of materials. XPS analysis was conducted on the 200 °C annealed sample due to some instrumental limitations. This sample exemplified the extreme annealing condition, and compositional uniformity across other samples was corroborated by EDX analysis. Fig. 6(a) illustrates the S 2p core-level spectrum of the Bi_2S_3 film in the 158–167 eV binding energy range. The S 2p core-level spectrum consists of two subpeaks corresponding to S $2p_{1/2}$ and S $2p_{3/2}$ states. This can be found from the deconvoluted spectrum. The peak at 162.1 eV corresponds to the S^{2-} state. The core-level spectrum of Bi 5d shows a peak at 25.6 eV and two subpeaks corresponding to Bi $5d_{3/2}$ and Bi $5d_{5/2}$ of the Bi^{3+} oxidation state, which can be obtained after the deconvolution of the main peak.[40]

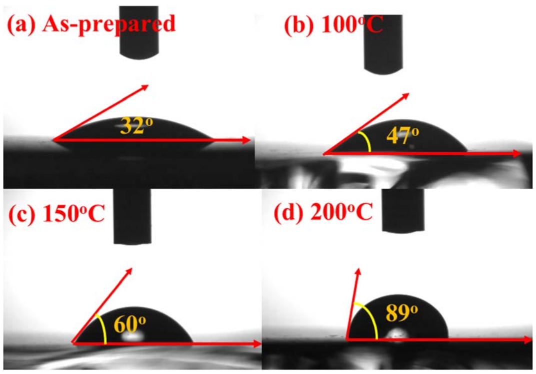

Fig. 7 Contact angle data of the (a) as-prepared, (b) 100 °C annealed, (c) 150 °C annealed, (d) 200 °C annealed Bi_2S_3 films.

3.2. Surface wettability analysis

The behaviour of any film surface towards liquid is probed through a surface wettability study. It links the surface morphology between liquid and solid surfaces in contact. It is analysed through contact angle data. If the contact angle (θ_c) is less than 90°, the surface is hydrophilic, whereas if it is more than 90°, the surface is hydrophobic.[41,42] A hydrophilic film attracts water molecules, whereas a hydrophobic film repels them.

As shown in Fig. 7(a), the θ_c of the as-prepared film is 32°, indicating the hydrophilic nature of the film. The value of θ_c is found to increase upon annealing and is found to be 89 °C for the 200 °C annealed film (Fig. 7(d)). The θ_c values of the 100 °C and 150 °C annealed films are 47 °C and 60°, respectively. This indicates a reduction in hydrophilicity as the contact angle value increases upon annealing. The surface wettability becomes hydrophobic one. The interaction strength between the solid and liquid surfaces was calculated using the surface free energy (γ_{se}). It was evaluated by the Young equation:[43] $\gamma_{se} = \dfrac{\gamma_w(1+\cos\theta_C)^2}{4}$, where $\gamma_w = 71.99$ Nm m^{-1} (water surface tension). The calculated γ_{se} are listed in Table 2. Another important wettability parameter, the work of adhesion (W_{sl}), was computed using the Young–Dupre relation, $W_{sl} = \gamma_w(1 + \cos\theta_C)$. The values are listed in Table 2, indicating a decrease in the work of adhesion. The decreased hydrophilicity results in decreased surface roughness, making the surface water-repellent. Hydrophilic surfaces are highly useful in various applications, including biomedical applications, antifogging devices, and self-cleaning surfaces.[44–46]

Table 2 Surface wettability parameters of Bi_2S_3 films

Samples	θ_C (degree)	γ_{se} (mN m^{-1})	W_{sl} (mN m^{-1})
Asp	32	61.466	133.041
100 °C	47	50.917	121.087
150 °C	60	40.494	107.985
200 °C	89	18.631	73.246

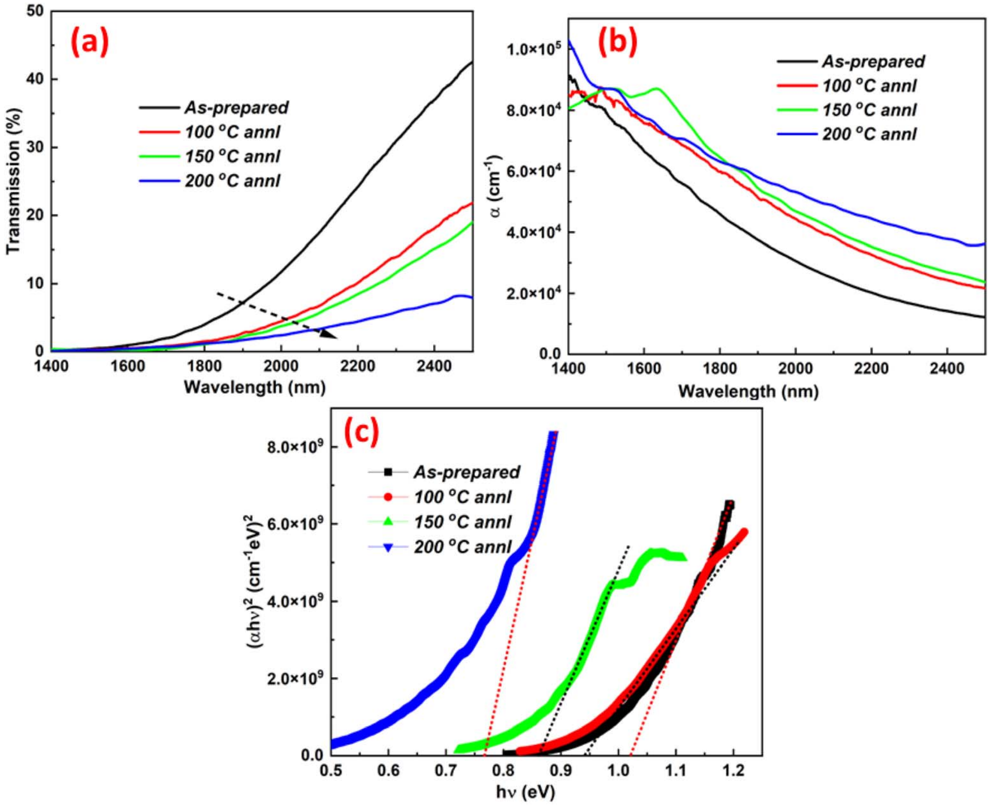

Fig. 8 (a) Transmittance, (b) absorption, (c) bandgap of Bi_2S_3 films annealed under different conditions.

3.3. Optical study

For optoelectronic device fabrication, one of the key factors is the optical properties of the films. The tuning of optical properties by thermal annealing makes it more useful for optoelectronic application. Optical transmission is a basic property that represents the transmitting power of light through a film. Fig. 8(a) illustrates the optical transmission of the Bi_2S_3 films after annealing under different conditions, as well as the as-prepared film. The highest transmission at 2500 nm of the as-prepared Bi_2S_3 film is ~43%, which systematically reduces upon annealing. The 200 °C annealed film shows a transmittance of ~8%.[48] The reason for this reduction in transmission is due to the increased number of defect states in band gap region, which prevents light from passing through.[36] The absorption edge is found to shift to a longer-wavelength regime, showing a reduction in the energy gap (E_g). The reduction in transmission is also due to increased light absorption, as evident from the enhanced absorption coefficient (α), as illustrated in Fig. 8(b). The α value was calculated using the equation.$\alpha = \left(\frac{1}{t}\right)\ln\left(\frac{1}{T}\right)$.[47] Here, t refers to the film thickness, and T stands for transmission. The E_g was determined from the Tauc equation at larger α values using the following equation:

Table 3 Optical parameters of Bi_2S_3 films annealed under different conditions

Optical parameter	As-prepared	100 °C	150 °C	200 °C
E_g (eV)	1.022	0.938	0.861	0.766
Tauc parameter ($\times10^{10}$, cm^{-1} eV)^2	3.14	2.96	2.75	2.63
Urbach energy (E_u, meV)	519	532	563	581
$\sigma(\times10^{-2})$	4.981	4.859	4.591	4.449
S_{e-p}	13.384	13.721	14.521	14.984
η_{opt}	1.661	1.651	1.640	1.626
ε_∞	11.269	11.847	12.453	13.329
n_0	3.357	3.442	3.529	3.651
χ^1 (esu)	0.817	0.863	0.912	0.981
χ^3 ($\times10^{-11}$ esu)	7.574	9.429	11.761	15.744
n_2 ($\times10^{-10}$ esu)	8.501	10.322	12.557	16.248

$$(\alpha h\nu) = C(h\nu - E_g)^y \tag{2}$$

The exponent y in eqn (2) indicates the type of transition occurring between the valence and conduction bands. The value of $y = 2$, 1/2 is for indirect allowed and direct allowed transitions. Y = 3/2 and 3 refer to direct and indirect forbidden transitions, respectively. In the present case, $y = 1/2$ fits well with the experimental data, which indicates a direct allowed transition occurring in the films. Thus, the optical bandgap was determined using the Tauc relation assuming a direct allowed transition ($y = 1/2$), and the bandgap (E_g) values of the films were obtained from the linear region (x-intercept of the fitting) of the $(\alpha h\nu)^2$ *vs.* $h\nu$ plot, as shown in Fig. 8(c) and presented in Table 3. The bandgap of the as-prepared Bi_2S_3 film is well supported by the DFT calculations (~0.9823), close to the experimental value. The E_g value decreases from 1.022 eV for the unannealed film to 0.766 eV for the 200 °C annealed film. It is explained by Davis and Mott, the so-called "density of state model".[49]

The reduction in the E_g value is due to the annealing-induced structural modification in the film, as evident from the XRD data. The constant C in eqn (2) is the Tauc parameter. It evaluates the degree of disorder/order in the films. The values also decrease upon annealing, as depicted in Table 3. This signifies increased disorder in the film upon annealing. The change in E_g by disorder or defect states was well measured using the Urbach energy (E_u) using the relation:[50]

$$\alpha = \alpha_0 \exp\left(\frac{h\nu}{E_U}\right) \tag{3}$$

The observed lower bandgap, in contrast to bulk Bi_2S_3 (1.3–1.7 eV), is ascribed to defect-induced band tailing, non-stoichiometry, and annealing-induced structural disorder, as indicated by elevated Urbach energy and lattice strain, which create localized states within the bandgap. The obtained E_u values for the different film samples are presented in Table 3. The as-deposited Bi_2S_3 film has an E_u value of 519 meV, which increases to 581 meV upon annealing at 200 °C. The increased disorder is clearly from the increased value of E_u upon annealing. The relatively high E_u values (519–581 meV) show that the films have a lot of structural disorder and defect-induced band tailing. This is because thermally evaporated thin films have a nanocrystalline structure, grain boundary defects, and possibly nonstoichiometry, which causes a high density of localized states in the bandgap.

The other two E_u-dependent parameters, σ (steepness parameter) and S_{e-p} (electron–phonon interaction strength), are evaluated as follows:[47]

$$\sigma = \frac{K_B T}{E_U} \text{ and } S_{e-p} = \frac{2}{3\sigma} \tag{4}$$

The reduction in σ from 4.981×10^{-2} to 4.449×10^{-2} presents a steeper absorption edge, which is seen from Fig. 8(b). At the same time, the S_{e-p} value increases from 13.384 to 14.984 after 200 °C annealing (Table 3). The variation is presented in Fig. S2. It implies that electron–phonon coupling is strengthened by annealing. The improved S_{e-p} presents optimised lattice vibration.

The skin depth (δ) is associated with α by the equation $\delta = 1/\alpha$. It is the depth at which the photon density decreases to 1/eth of its surface value. It is strongly related to the electrical conductivity of semiconducting materials, and its influence is also observed in the increased photocurrent value after annealing, as discussed in the following section. As depicted in Fig. 9(a), the skin depth decreases with increasing annealing temperature. The lower skin depth of the annealed film is due to its higher absorbance and reduced light transmittance, allowing less light to penetrate. In contrast, the as-prepared film shows higher transmittance and thus a larger skin depth.[52]

The energy lost by electromagnetic waves while moving through the film is represented by the extinction coefficient (k). It represents the amount of optical loss within the sample. It is computed by the formula.$k = \frac{\alpha\lambda}{4\pi}$[51] The combined effect of incident photon absorption and reflection at a particular λ is measured through this parameter. Fig. 9(b) illustrates the change in k with the wavelength. The k value decreases with the wavelength and increases with annealing temperatures.

The optical density (OD) is a measure of the extent to which light is absorbed by a film. It is directly related to the film thickness (t) and determined using the equation OD = $\alpha \times t$.[51] Fig. 9(c) illustrates the change in the OD with the wavelength at different annealing states. The OD value decreases with the wavelength and increases with the annealing temperatures.

The refractive indices (n) of these samples were evaluated theoretically from E_g values using various models, as presented in Fig. 9(d). The different theoretical models used for the calculations are as follows:

$$\frac{{n_0}^2 - 1}{{n_0}^2 + 2} = 1 - \sqrt{\frac{E_g}{20}} \tag{5a}$$

by Dimitrov–Sakka ref. 53.

$$n_T = 1.73\times(1 + 1.9017 \times e^{-(0.539 \times E_g)} \tag{5b}$$

by Tripathy ref. 54.

$$n_M = \left(\frac{95}{E_g}\right)^{1/4} \tag{5c}$$

by Moss ref. 55

$$n_R = 4.084 - 0.62 \times E_g \tag{5d}$$

by Rabindra ref. 56

$$n_{HV} = \sqrt{1 + \left(\frac{13.6}{E_g + 3.47}\right)^2} \tag{5e}$$

by Herve and Vandamme.[57]

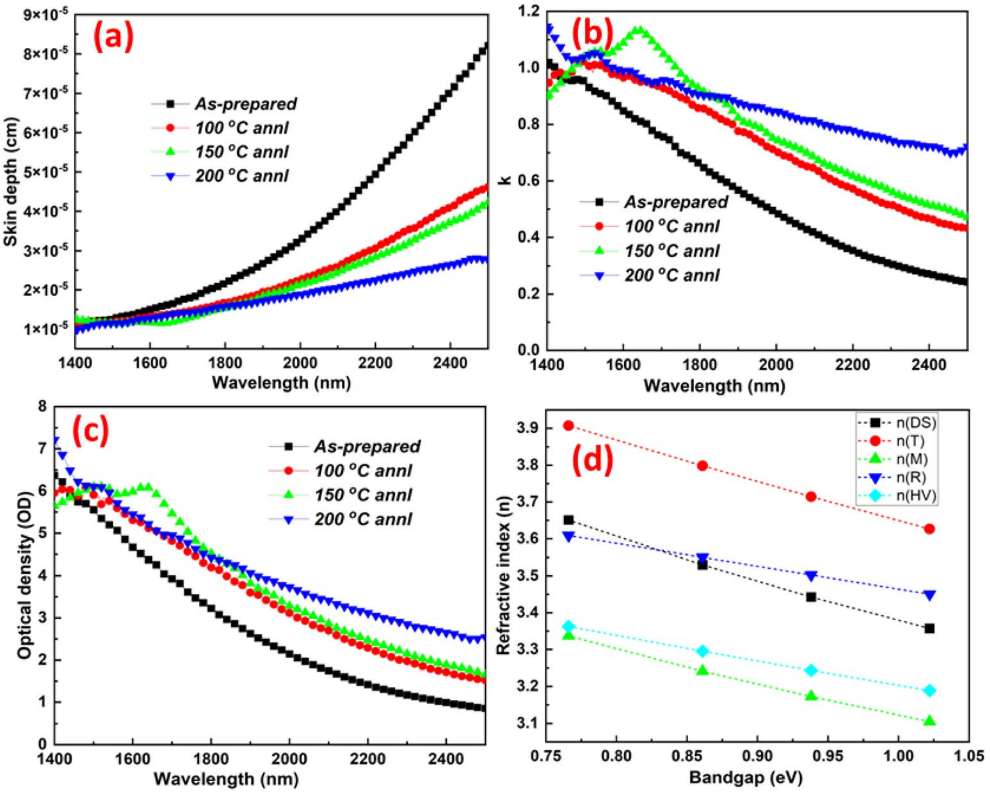

Fig. 9 (a) δ, (b) k, (c) OD and (d) refractive index of Bi_2S_3 films annealed under different conditions.

The n values obtained from these models are presented in Fig. 9(d), which indicates an increase in n with decreasing E_g. This increase in n implies enhanced optical performance, including extended photon path lengths, light trapping, reduced reflection losses, and suitability for integration in advanced tandem solar cell architectures.[58] Additionally, the optical electronegativity (ηopt) was calculated using the formula $\eta_{\text{opt}} = \left(\frac{C}{n_0}\right)^{1/4}$, and the values decrease upon annealing compared to their as-prepared state. The high-frequency dielectric constant was evaluated from the static refractive index using the relation $\varepsilon_\infty = {n_0}^2$. The dielectric constant is found to increase with the annealing temperature.

3.4. Nonlinear optical property analysis

The nonlinear optical properties shown by chalcogenide thin films are remarkable. This is due to their high refractive index, low phonon energy, and large third-order susceptibility. The nonlinear optical response of a material becomes evident under sufficiently intense irradiation and is strongly influenced by the applied electric field. This induces nonlinear effects within the films. The electronic polarizability, which occurs when the interaction between the electric field and the atomic nuclei takes place, results in modifications to bond lengths. The polarisation density, P, is expressed as a power series of the applied electric field:[59]

$$P = \varepsilon_0 \chi^E = \varepsilon_0[\chi^{(1)}E + \chi^{(2)}E^2 + \chi^{(3)}E^3] \tag{6a}$$

Here, E denotes the electric field intensity, while $\chi^{(1)}$ represents the linear response of the material. The coefficients $\chi^{(2)}$ and $\chi^{(3)}$ correspond to the second and third-order nonlinear susceptibilities, respectively. For optically isotropic materials with centrosymmetric structures, the second-order nonlinear susceptibility term, $\chi^{(2)}$, becomes zero.[60] It makes the third-order susceptibility, $\chi^{(3)}$, a dominant contributor to nonlinear effects. Hence, the values of $\chi^{(1)}$ and $\chi^{(3)}$ for the semiconductor films were determined using Miller's rule[61] as follows:

$$\chi^{(1)} = \frac{{n_0}^2 - 1}{4\pi} \tag{6b}$$

$$\chi^{(3)} = A\left(\frac{{n_0}^2 - 1}{4\pi}\right)^4 = A\left(\chi^{(1)}\right)^4 \tag{6c}$$

Here, $A = 1.7 \times 10^{-10}$ esu, and n_0 represents the static refractive index at $h\nu \rightarrow 0$. The values of $\chi^{(1)}$ and $\chi^{(3)}$ are presented in Table 3. It is evident that both $\chi^{(1)}$ and $\chi^{(3)}$ increase with the annealing temperature, which can be attributed to an increase in n_0. Miller's rule was employed to estimate the third-order nonlinear susceptibility, as Bi_2S_3 is a centrosymmetric semiconductor where χ^3 dominates, and the rule provides a reliable approximation based on the experimentally obtained refractive index. Generally, higher optical susceptibility is associated with a reduced band gap, increased polarizability, and a higher material density.[40] The enhancement in nonlinear susceptibility indicates the potential of these materials for application in compact, low-power photonic and telecommunication

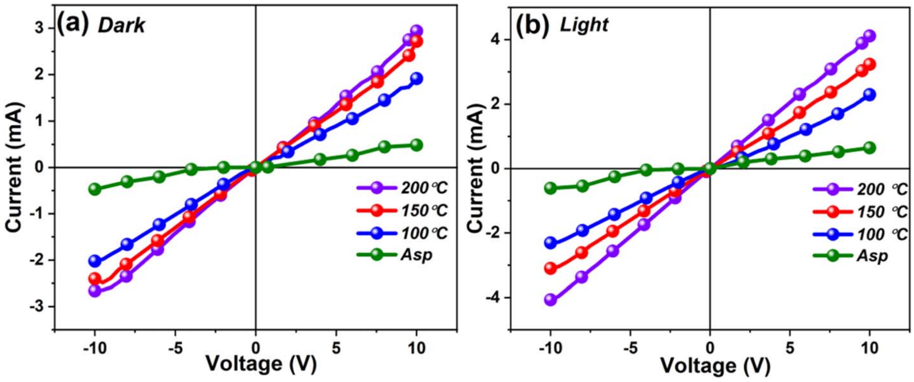

Fig. 10 *I–V* characteristic plots of all Bi_2S_3 thin films under (a) dark and (b) illuminated conditions.

Table 4 Photoresponse characteristic parameters of Bi_2S_3 thin films

Samples	I_L (A)	I_D (A)	I_L–I_D (A)	Photosensitivity (%)	Responsivity (R) (A W^{-1})	Detectivity (D) (Jones)
Asp	6.42×10^{-4}	4.82×10^{-4}	1.60×10^{-4}	24.95	0.129	5.17×10^{9}
100 °C	2.29×10^{-3}	1.91×10^{-3}	3.74×10^{-4}	16.34	0.458	9.25×10^{9}
150 °C	3.23×10^{-3}	2.72×10^{-3}	5.15×10^{-4}	15.93	0.647	1.09×10^{10}
200 °C	4.11×10^{-3}	2.94×10^{-3}	11.8×10^{-4}	28.58	0.822	1.34×10^{10}

devices.[62] The variation of E_g and $\chi^{(3)}$, as illustrated in Fig. S3, shows an inverse relationship with the annealing temperature. Table S1 depicts the comparison of $\chi^{(3)}$ values for Bi_2S_3 or similar chalcogenides, showing that the obtained $\chi^{(3)}$ values are comparable to the reported values.

According to the relation proposed by Ticha and Tichy,[61] the nonlinear refractive index (n_2) is expressed in terms of $\chi^{(3)}$ and n_0 as follows:

$$n_2 = \frac{12\pi\chi^{(3)}}{n_0} \tag{6d}$$

The improved behaviour is attributed to enhanced polarizability, which leads to higher refractive index values.[63] The improvements in nonlinear parameters are attributed to increased material homogeneity, polymerisation, and local structural modifications induced by thermal annealing. Such improvements highlight the suitability of the studied films for photonic applications, including high-performance electro-optic switches and related devices.

The optical parameters obtained through semiempirical models are inherently approximate and depend on simplifying assumptions. Thus, the derived values ought to be regarded as qualitative assessments beneficial for comparative analysis rather than precise quantification.

3.5. Photoresponse behaviour

To design and develop optoelectronic devices and to understand the electrical behaviour of materials, photo-response studies are essential. The *I–V* change of the films under study is shown in Fig. 10. The *I–V* plots under dark (Fig. 10(a)) and illuminated (Fig. 10(b)) conditions exhibit nearly linear and symmetric behaviour for all samples, indicating ohmic contacts between the electrodes and the thin films. This confirms efficient charge injection and transport without significant Schottky barriers. The as-deposited film possesses the lowest dark current, whereas the annealed samples show a systematic increase in the dark current with increasing annealing temperature. A similar behaviour is also seen under the illumination condition. However, upon illumination, all samples exhibit a pronounced increase in the current compared to the dark condition, as illustrated in Fig. S4, confirming good photoresponse behaviour. The photocurrent increases significantly with the annealing temperature, with the highest response observed for the 200 °C annealed film. Such an enhancement stems from the efficient generation of electron–hole pairs, reduced recombination losses, and improved carrier transport resulting from light-matter interactions.[64–67] The difference between illuminated and dark currents (I_L–I_D), which represents the net photogenerated current, shows a continuous rise from 1.60×10^{-4} A (the as-prepared film) to 11.8×10^{-4} A (the 200 °C annealed film). This confirms that annealing facilitates better charge transport. The parameters for measuring the photodetection properties of a material are photosensitivity (S), detectivity (D), and responsivity (R). These parameters were derived from the maximum values of the dark current (I_D) and light current (L) by the following equations (eqn (7))[67,68] and are tabulated in Table 4.

$$\text{Photosensitivity}(S\%) = \frac{I_L - I_D}{I_L} \times 100 \tag{7a}$$

$$\text{Responsivity}(R) = \frac{I_\text{L}}{A \times P_\text{in}} \tag{7b}$$

$$\text{Detectivity}(D) = R\sqrt{\frac{A}{2\text{e}I_\text{D}}} \tag{7c}$$

In this case, e stands for the elementary charge of an electron, P_in is the incident light power density (20 mW cm^{-2}), and A is the sample area, which is roughly 0.25 cm^{-2}.

Although the photosensitivity initially decreases at 100 °C and 150 °C, it reaches a maximum of 28.58% at 200 °C, indicating that higher annealing temperatures enhance light-matter interactions and carrier mobility.

Responsivity is a crucial parameter for evaluating the performance of photodetectors and optoelectronic devices, as it determines how efficiently the device translates the incident optical power into the corresponding electrical output signal. A similar trend is observed in the responsivity (R), which increases markedly from 0.129 A W^{-1} (the as-prepared film) to 0.822 A W^{-1} (the 200 °C annealed film). This nearly seven-fold improvement signifies that the annealed films convert incident photons into an electrical signal much more efficiently.

Detectivity is a crucial parameter for evaluating a photodetector's performance, as it indicates the device's capability to sense weak optical signals with noise. The detectivity also increases steadily, reaching 1.34 × 10^{10} Jones at 200 °C, confirming reduced noise levels and an improved signal-to-noise ratio. The rise in detectivity indicates superior sensitivity to weak optical signals in the annealed samples. Overall, the *I–V* characteristics demonstrate that annealing significantly improves the photocurrent, responsivity, and detectivity, establishing the 200 °C annealed film as the most efficient photodetector among the studied samples. These results suggest that optimised thermal treatment enhances responsivity and detectivity, making the films suitable for photodetector applications.

4. Density functional theory analysis

4.1. Computational methods

DFT calculations, based on the full-potential linearised augmented plane wave (FP-LAPW) method, as implemented in the MedeA-VASP framework, were performed to investigate the structural stability, electronic structure, and optical response of the layered Bi_2S_3 structure.[69,70] A slab model of layered Bi_2S_3 was constructed by cleaving the crystal along the (112) crystallographic direction, with a 15 Å vacuum spacing along the *z*-axis to avoid interactions between periodically repeated layers. The structural model was generated and cleaved using the VESTA visualization software.[71] The influence of the exchange–correlation was preserved by generalized gradient approximation (GGA) with the Perdew–Burke–Ernzerhof (PBE) function.[72] A plane-wave cutoff energy of 600 eV and a 4 × 4 × 1 Monkhorst–Pack grid were employed to ensure convergence of the total energies and electronic properties. Structural optimizations were performed until the forces on each atom were below 0.001 eV Å^{-1} and the total energy converged to 10^{-6} eV.[73] The self-consistent field (SCF) calculations were considered converged when the total energy difference between successive iterations was less than 10^{-6} eV. To improve convergence near the Fermi level, Gaussian smearing with a width of 0.005 eV was applied.

4.2. Electronic structure

The electronic properties of layered Bi_2S_3 were examined *via* band structure and density of states analyses, as shown in Fig. 11(a). The calculated band structure along the high-symmetry path *F*–Γ–*B*–*G*–Γ reveals a bandgap of 0.9823 eV, indicating a semiconducting nature. Projected DOS indicates that the valence band is dominated by S 3p states, while the conduction band primarily arises from Bi 6p orbitals. The two-dimensional charge density contour map further illustrates the distribution of electronic charges in the Bi_2S_3 layered structure. These analyses provide a clear understanding of Bi_2S_3's electronic behaviour, underpinning its potential for optoelectronic applications. Defect states caused by structural disorder and nonstoichiometry create localized energy levels within the bandgap. This lowers the effective bandgap by making it easier

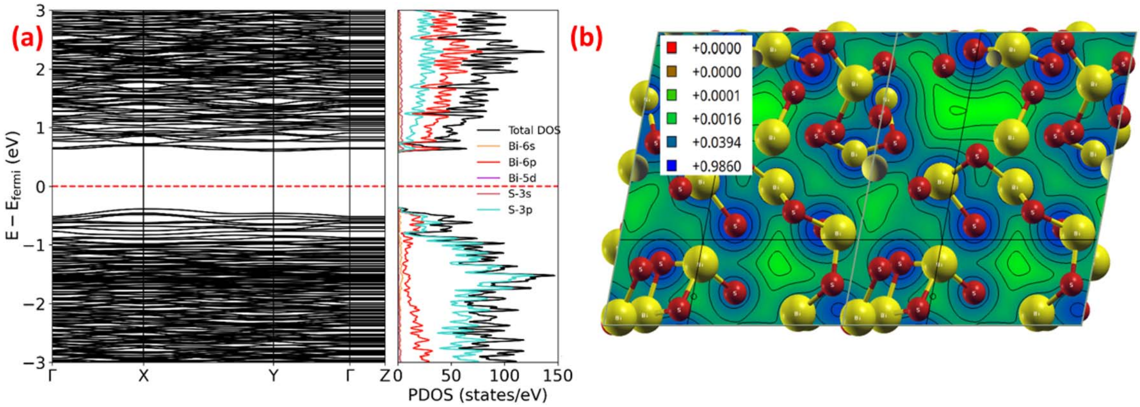

Fig. 11 (a) Calculated band structures and corresponding density of state of the Bi_2S_3 layer structure. (b) Two-dimensional contour plot for the charge density map of the Bi_2S_3 layer structure.

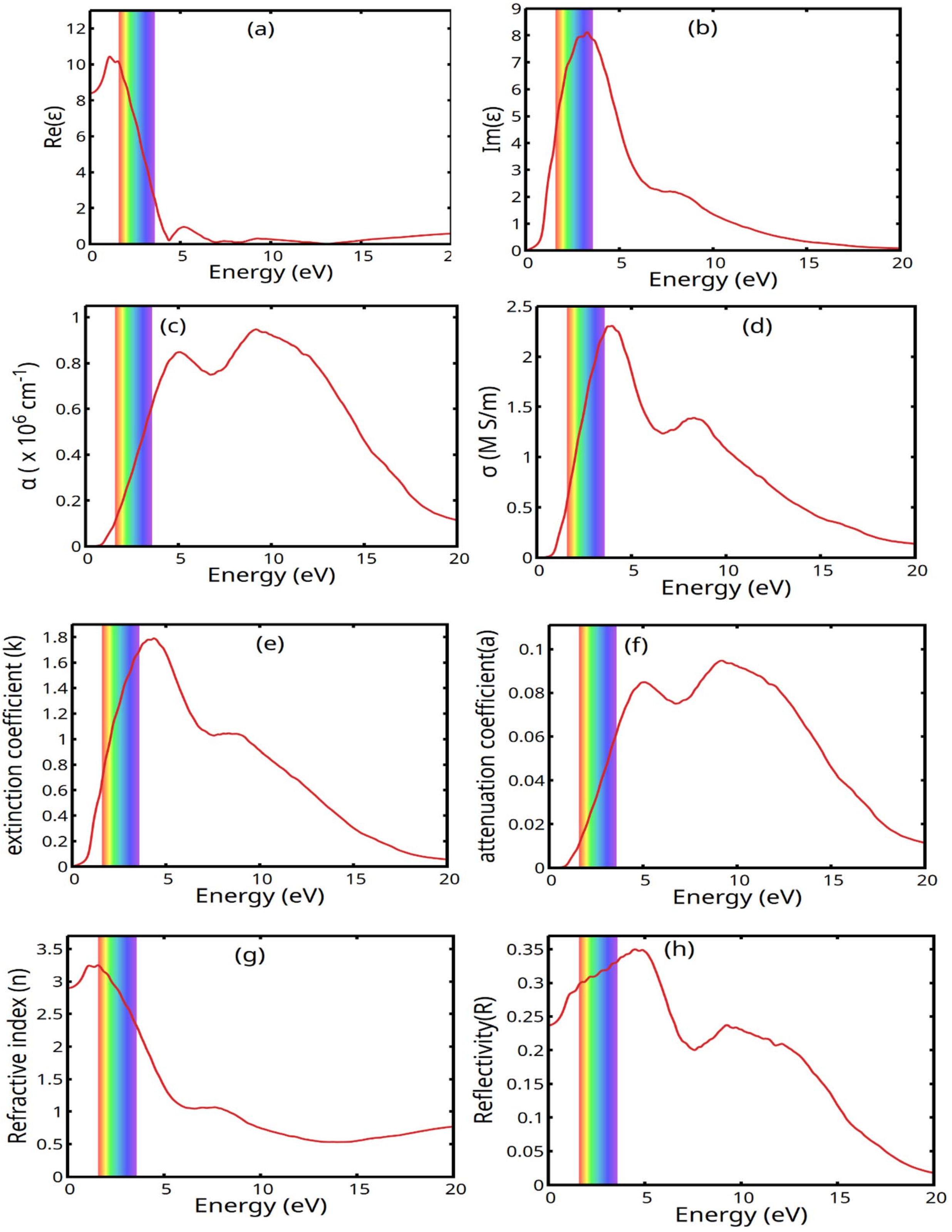

Fig. 12 Optical characteristics of the Bi_2S_3 layered structures: (a and b) real and imaginary parts of the dielectric function, (c) absorption coefficient, (d) optical conductivity, (e) extinction coefficient, (f) attenuation coefficient, (g) refractive index, and (h) reflectivity.

for electrons to move between bands, which was seen in experiments. A contour map of the charge density plot is shown in Fig. 11(b), indicating that more charges are concentrated in the Bi atoms.

4.3. Optical properties

The optical response of Bi_2S_3 was systematically investigated within the framework of density functional theory by first evaluating the frequency-dependent complex dielectric function. All other optical parameters were subsequently derived from this frequency-dependent dielectric function. The frequency-dependent variation of these dielectric components in the photon energy range of 0–20 eV is illustrated in Fig. 12(a–h). The real part of the dielectric function, $\mathrm{Re}(\varepsilon)$, as shown in Fig. 12(a), represents the dispersive response of the material to an external electromagnetic field and provides information on the polarisation behaviour. The static dielectric constant represents the low-frequency dielectric response and reflects the inherent polarisation of the material, which is calculated to be 8.418 for the Bi_2S_3 structure. The significant value of the static dielectric constant implies enhanced polarisation, which is favourable for device performance. The $\mathrm{Re}\{\varepsilon(\omega)\}$ value increases in the low-energy region and reaches a peak value of 10.447 for Bi_2S_3, signifying enhanced polarisation at low frequencies, followed by a gradual decline as the photon energy increases. The imaginary part of the dielectric function, $I_m(\varepsilon)$, arises from interband electronic transitions between occupied and unoccupied states. The features observed in the imaginary part of the dielectric function correspond well with the electronic density of states, as shown in Fig. 11(a). The main peaks in $I_m(\varepsilon)$ originate from interband electronic transitions identified in the DOS. Consequently, the major peaks in $I_m(\varepsilon)$ originate from optical transitions between S 3p valence states and Bi 6p conduction states, confirming the electronic origin of the optical absorption process. The absorption coefficient, $\alpha(\omega)$, derived from the complex dielectric function, measures the extent to which incident photons are absorbed within the material. It increases sharply with the photon energy, reaching a peak before gradually decreasing, as fewer electronic states are available for transitions at higher energies (Fig. 12(c)). Fig. 12(d) shows the optical conductivity spectra, $\sigma(\omega)$, with a peak value of 3.948 at a lower photon energy value. The extinction coefficient, $\kappa(\omega)$, and the attenuation coefficient, $a(\omega)$, in Fig. 12(e and f), respectively, together provide insights into optical losses and energy dissipation inside the Bi_2S_3 structure, which are critical for designing efficient optical and photonic devices. The Bi_2S_3 layered structure shows a pronounced refractive index, indicating significant optical polarisation and a relatively high electronic density of states near the Fermi level (Fig. 12(g)). The reflectivity spectra (Fig. 12(h)) provide information on the fraction of incident light reflected by the material surface. The Bi_2S_3 structure exhibits a maximum reflectance of 23.7% at a photon energy of 0 eV. These optical properties clearly connect the electronic structure to light-matter interactions.

5. Conclusion

The Bi_2S_3 film with a ~700 nm thickness exhibited significant changes in various properties upon thermal annealing at different temperatures. The average crystallite size reduced to 25.21 nm upon 200 °C annealing, which enhanced the lattice strain to 8.97×10^{-3} from 6.34×10^{-3}. The dislocation density increased to 1.57×10^{-3} upon annealing. The presence of bismuthinite phases with the (321), (021), and (200) planes was seen in the XRD pattern, which is well supported by the SAED pattern and HRTEM fringes. The cross-sectional FESEM images confirmed the change in the surface morphology with annealing, and the decrease in the particle was also evident from the FESEM images. The XPS study indicated the oxidation states of Bi^{3+} and S^{2-} in Bi_2S_3, along with elemental confirmation, which is also supported by the EDX spectra. The contact angle increased from 32° to 89° upon annealing, indicating a reduction in the hydrophilicity of the annealed film. The bandgap reduction from 1.022 eV to 0.766 eV upon annealing at 200 °C resulted in an increase in the refractive index from 3.357 to 3.651 and a decrease in the optical electronegativity from 1.661 to 1.626. The third-order nonlinear susceptibility increased by two-fold (from 7.574×10^{-11} esu to 15.744×10^{-11} esu) as along with a two-fold increase in the nonlinear refractive index (from 8.501×10^{-10} esu to 16.248×10^{-10} esu). The photocurrent, which was found to be in the mA range, also increased upon annealing, and the photodetectivity increased from 5.17×10^9 to 1.34×10^{10} Jones with a simultaneous increase in the responsivity from 0.129 to 0.822 A W^{-1} upon 200 °C annealing. The theoretical study provided strong support for the experimental findings in terms of their electronic structure and other optical parameters. The observed properties, including linear, nonlinear, and other structural and morphological characteristics, are suitable for various optoelectronic devices and white-light photodetectors.

Conflicts of interest

No conflicts of interest among the authors.

Data availability

The data are included in the manuscript and the supplementary information (SI). It can be obtained from the corresponding author upon request. Supplementary information: EDX of annealed films, variation in the steepness parameter and Se-p, variation in nonlinear parameters, *I–V* data for individual films, and comparison table of χ^3 values. See DOI: https://doi.org/10.1039/d6ra01732k.

Acknowledgements

The authors acknowledge the ICT-IOC central facility for various characterisations.

References

1 S. Sengupta, R. Aggarwal and M. Raula, A review on chemical bath deposition of metal chalcogenide thin films for heterojunction solar cells, *J. Mater. Res.*, 2023, **38**, 142–153.
2 J. W. Turnley and R. Agrawal, Solution-processed metal chalcogenide semiconductors for inorganic thin film photovoltaics, *Chem. Commun.*, 2024, **60**, 5245–5269.

3 F. Wang, Y. Zhang, Y. Gao, P. Luo, J. Su, W. Han and K. Liu, 2D metal chalcogenides for IR photodetection, *Small*, 2019, **15**(30), 1901347.

4 P. Priyadarshini, S. Das and R. Naik, A review on metal-doped chalcogenide films and their effect on various optoelectronic properties for different applications, *RSC Adv.*, 2022, **12**, 9599–9620.

5 S. Mohapatra, H. T. Das, B. C. Tripatshy and N. Das, Recent developments in electrodeposition of transition metal chalcogenides-based electrode materials for advanced supercapacitor applications: A review, *Chem. Rec.*, 2024, **24**(1), 202300220.

6 K. Rodríguez-Rosalesa, J. Cruz-Gomez, J. S. Cruzb, A. Guillén-Cervantesd, F. de Moure-Floresb and M. Villagrán-Muniz´an-Muniz, Plasma emission spectroscopy for studying Bi_2S_3 produced by pulsed laser deposition and effects of substrate temperature on structural, morphological, and optical properties of thin films, *Mater. Sci. Eng., B*, 2025, **312**, 117867.

7 H. Song, X. Zhan, D. Li, Y. Zhou, B. Yang, K. Zeng, J. Zhong, X. Miao and J. Tang, Rapid thermal evaporation of Bi_2S_3 layer for thin film photovoltaics, *Sol. Energy Mater. Sol. Cells*, 2016, **146**, 1–7.

8 G. Konstantatos, L. Levina, J. Tang and E. H. Sargent, sensitive solution-processed Bi2S3 nanocrystalline photodetectors, *Nano Lett.*, 2008, **8**, 4002–4006.

9 R. Chmielowski, D. P. C. Bera, I. Opahle, W. Xie, S. Jacob, F. Capet and G. Dennler, Theoretical and experimental investigations of the thermoelectric properties of Bi_2S_3, *J. Appl. Phys.*, 2015, **117**, 125103.

10 B. Chitara, B. S. C. Kolli and F. Yan, Near-Infrared photodetectors based on 2D Bi2S3, *Chem. Phys. Lett.*, 2022, **804**, 139876.

11 Y. Yu, Z. Hu, S. Y. Lien, Y. Yu and P. Gao, Self-Powered thermoelectric hydrogen sensors based on low-cost bismuth sulfide thin films: Quick response at room temperature, *ACS Appl. Mater. Interfaces*, 2022, **14**, 47696–47705.

12 U. Chalapathi, B. P. Reddy, R. Dhanalakshmi, G. S. Reddy, A. Divya, S. Sangaraju, S. Alhammadi, K. Mohanarangam, A. A. A. Bahajjaj and S. H. Park, Seed layer-assisted growth of Bi_2S_3 nanorod films for efficient photoelectrochemical water splitting, *Int. J. Hydrogen Energy*, 2025, **101**, 1085–1092.

13 S. S. Raut, J. A. Dhobale and B. R. Sankapal, SILAR deposited Bi_2S_3 thin film towards an electrochemical supercapacitor, *Phys. E*, 2017, **87**, 209–212.

14 S. S. Kumar, S. Valanarasu, M. A. Manthrammal and M. Shkir, Effect of coating temperature on the physical properties of Bi_2S_3 thin films for photodetector applications, *J. Mater. Sci.: Mater. Electron.*, 2024, **35**, 195.

15 P. Rong, S. Gao, L. Li, W. He, M. Zhang, S. Ren, Y. Han, S. Jiao, Q. Chen and J. Wang, Surface engineering of highly ordered Bi_2S_3 film with open channels toward high-performance broadband photodetection, *InfoMat*, 2024, **6**(11), 12567.

16 E. Pineda, M. E. Nicho, P. K. Nair and H. Hu, Optoelectronic properties of chemically deposited Bi_2S_3 thin films and the photovoltaic performance of Bi_2S_3/P_3OT solar cells, *Sol. Energy*, 2012, **86**, 1017–1022.

17 K. R. Rosales, J. C. Gómez, J. S. Cruz, A. G. Cervantes, F. de Moure-Flores and M. V. Muniz, Plasma emission spectroscopy for studying Bi_2S_3 produced by pulsed laser deposition and effects of substrate temperature on structural, morphological, and optical properties of thin films, *Mater. Sci. Eng., B*, 2025, **312**, 117867.

18 M. Bouachri, H. El Farri, M. Beraich, M. Taibi, K. Nouneh and M. Fahoum, Influence of cycle numbers on optical parameters of nanostructured Bi_2S_3 thin films using SILAR method for solar cells light harvesting, *Materialia*, 2021, **20**, 101242.

19 G. Xie, Z. P. Qiao, M. H. Zeng and X. M. Chen, A Single-Source approach to Bi_2S_3 and Sb_2S_3 nanorods via a hydrothermal treatment, *Cryst. Growth Des.*, 2004, **4**, 513–516.

20 M. Medles, N. Benramdane, A. Bouzidi and A. Nakrela, Optical and electrical properties of Bi2S3 films deposited by spray pyrolysis, *Thin Solid Films*, 2006, **497**, 58–64.

21 F. Tezcan, A new synthesis route of Bi2S3 with solvothermal deposition in photoelectrochemical hydrogen production, *J. Mol. Struct.*, 2024, **1301**, 137418.

22 A. Jana, P. Hazra, M. Hazra and J. Datta, Sequential electrodeposition of Bi2S3/CdS films as co-sensitiser photoanodes for liquid junction solar cell, *Mater. Chem. Phys.*, 2016, **183**, 173–180.

23 S. ten Haaf, H. Sträter, R. Brüggemann and G. H. Bauer, Physical vapour deposition of Bi2S3 as absorber material in thin film photovoltaics, *Thin Solid Films*, 2013, **535**, 394–397.

24 C. Lu, M. Luo, Y. Ge, Y. Huang and Q. Zhao, layer-dependent nonlinear optical properties of WS_2, MoS_2, and Bi_2S_3 films synthesized by chemical vapor deposition, *ACS Appl. Mater. Interfaces*, 2021, **14**(1), 2390–2400.

25 P. A. Chate and S. D. Lakde, Electrical, optical and structural properties of rod-shaped Bi2S3 thin films deposited by dip technique, *J. Mater. Sci.: Mater. Electron.*, 2015, **26**, 5847–5851.

26 A. Hussain, A. Begum and A. Rahman, Effects of annealing on nanocrystalline Bi2S3 thin films prepared by chemical bath deposition, *Mater. Sci. Semicond. Process.*, 2014, **21**, 74–81.

27 R. Panda, S. A. Khan, U. P. Singh, R. Naik and N. C. Mishra, The impact of fluence dependent 120 MeV Ag swift heavy ion irradiation on the changes in structural, electronic, and optical properties of AgInSe2 nano-crystalline thin films for optoelectronic applications, *RSC Adv.*, 2021, **11**(42), 26218–26227.

28 A. R. Barik, K. V. Adarsh, R. Naik, C. S. Sandeep, R. Philip, D. Zhao and H. Jain, Photoinduced transparency of effective three-photon absorption coefficient for femtosecond laser pulses in Ge16As29Se55 thin films, *Appl. Phys. Lett.*, 2011, **98**, 201111.

29 S. Ahmad, S. Islam, M. Nasir and K. Asokan, Effects of gamma-ray irradiation on the optical properties of

amorphous Se100-xHgx thin films, *J. Phys. Chem. Solids*, 2018, **117**, 122–130.

30 P. Priyadarshini, D. Alagarasan, R. Ganesan, S. Varadharajaperumal and R. Naik, Influence of Proton Ion Irradiation on the Linear–Nonlinear Optoelectronic Properties of Sb40Se20S40 Thin Films at Different Fluences for Photonic Devices, *ACS Appl. Opt. Mater.*, 2022, **1**(1), 55–68.

31 S. Giri, P. Priyadarshini, D. Alagarasan, R. Ganesan and R. Naik, Annealing-induced phase transformation in In10Se70Te20 thin films and its structural, optical and morphological changes for optoelectronic applications, *RSC Adv.*, 2023, **13**(36), 24955–24972.

32 E. L. Pankratov, Influence of the spatial, temporal, and concentrational dependence of the diffusion coefficient on dopant dynamics: optimization of annealing time, *Phys. Rev. B*, 2005, **72**, 075201.

33 R. P. Wang, S. J. Madden, C. J. Zha and A. V. Rode, Annealing-induced phase transformations in amorphous As_2S_3 films, *J. Appl. Phys.*, 2006, **100**, 063524.

34 P. A. Hind, P. S. Patil, N. B. Gummagol and B. V. Rajendra, Influence of annealing on microstructure, nonlinear optical and electrical properties of spray pyrolyzed $Sn_{0.97}La_{0.03}O_2$ films, *Opt. Mater.*, 2022, **125**, 112080.

35 S. Das, S. Senapati, D. Alagarasan, S. Varadharajaperumal, R. Ganesan and R. Naik, Enhancement of nonlinear optical parameters upon phase transition in new quaternary $Ge_{20}Ag_{10}Te_{10}Se_{60}$ films by annealing at various temperatures for optoelectronic applications, *J. Alloys Compd.*, 2022, **927**, 167000.

36 B. Mohanty, S. Das, P. C. Kumar, D. Alagarasan, R. Ganesan and R. Naik, Exploring the optical, structural, and surface wettability of thermally evaporated $Ag_{25}S_{35}Se_{40}$ thin films by annealing for optoelectronic applications, *Phys. B Condens. Matter*, 2025, **699**, 416823.

37 S. Das, S. Paikaray, I. Swain, S. Senapati and R. Naik, Tuning in linear and nonlinear optical parameters by interfacial mixing of Sb/Ag_2Se bilayer thin films under annealing at different temperatures for optoelectronic applications, *Surf. Interfaces*, 2023, **42**, 103395.

38 A. A. Akla and A. S. Hassanien, Microstructure and crystal imperfections of nanosized CdS_xSe_{1-x} thermally evaporated thin films, *Superlattices Microstruct.*, 2015, **85**, 67–81.

39 S. Saleem, A. H. Jabbar, M. H. Jameel, A. Rehman, Z. H. Kareem, A. H. Abbas, Z. Ghaffar, S. A. Razzaq, R. A. Pashameah, E. Alzahrani, E. P. Ng and S. M. Sapuan, Enhancement in structural, morphological, and optical properties of copper oxide for optoelectronic device applications, *Nanotechnol. Rev.*, 2022, **11**, 2827–2838.

40 G. Mallick, P. C. Kumar, R. Naik and R. Biswal, Enhanced photoresponse from Ag/Bi_2Se_3 heterostructure thin films under thermal annealing, *ACS Appl. Electron. Mater.*, 2025, **7**, 5583–5598.

41 S. Zhu, Q. Zhao, Y. Chen, M. S. Khan, C.-M. Chang, T.-S. Chung and S. B. Chen, Interface-Engineered Nanohybrid Membranes for Selective Boron Removal from Brackish Water and Seawater Reverse Osmosis Permeate, *Environ. Sci. Technol.*, 2026, **60**(2), 2160–2172.

42 S. Zhu, H. Xu, M. S. Khan, M. Xia, F. Wang and Y. Chen, Enhanced removal of Ni^{2+} and Co^{2+} from wastewater using a novel 2-hydroxyphosphonoacetic acid modified Mg/Fe-LDH composite adsorbent, *Water Res.*, 2025, **272**, 122997.

43 J.-Y. Wang, W.-H. Li, Z. Wei, C. Zhang, Y.-H. Li, G. Xu and S.-Q. Zang, A hydrophobic semiconducting metal–organic framework assembled from silver chalcogenide wires, *Chem. Commun.*, 2020, **56**, 2091–2094.

44 L. Mahapatra, P. C. Kumar, D. Alagarasan, C. Sripan and R. Naik, Laser-irradiated Ag/Sb20S40Se40 heterostructure film for enhanced photodetector application, *Mater. Chem. Phys.*, 2025, **348**, 131638.

45 P. A. Trzaskowska, A. Kuźmińska, B. Butruk-Raszeja, E. Rybak and T. Ciach, Electropolymerized hydrophilic coating on stainless steel for biomedical applications, *Colloids Surf. B Biointerfaces*, 2018, **167**, 499–508.

46 Y. Zhu, G. Guo, J. Lu, C. Ye, Y. Xie, Y. Lu and S. Tu, A transparent hydrophilic coating for long-lasting anti-fogging with self-cleaning and antibacterial properties, *Chem. Eng. J.*, 2024, **496**, 153773.

47 S. K Sethi and G. Manik, Recent progress in super hydrophobic/hydrophilic self-cleaning surfaces for various industrial applications: a review, *Polym.-Plast. Technol. Mater.*, 2018, **57**, 1932–1952.

48 R. Naik, S. K. Parida, C. Kumar, R. Ganesan and K. S. Sangunni, Optical properties change in Sb40S40Se20 thin films by light-induced effect, *J. Alloys Compd.*, 2012, **522**, 172–177.

49 S. Das, S. Senapati, D. Alagarasan, S. Varadhrajaperumal, R. Ganesan and R. Naik, Thermal Annealing-Induced Transformation of Structural, Morphological, Linear, and Nonlinear Optical Parameters of Quaternary $As_{20}Ag_{10}Te_{10}Se_{60}$ Thin Films for Optical Applications, *ACS Appl. Opt. Mater.*, 2023, **1**(1), 17–31.

50 N. F. Mott and E. A. Davis, in, *Electronic Processes in Non-crystalline Materials*, Clarendon Press, Oxford, 1979, pp. 210.

51 F. Urbach, The long-wavelength edge of photographic sensitivity and of the electronic absorption of solids, *Phys. Rev.*, 1953, **92**, 1324.

52 S. Giri, P. C. Kumar, S. Supriya, D. Alagarasan and R. Naik, Enhanced Photodetectivity and responsivity in In10Se70Te15Bi5 film by time-dependent laser irradiation for photodetector applications, *RSC Adv.*, 2025, **15**, 46821–46837.

53 A. Sharmin, S. S. Mahmood, M. Sultana, S. Aziz, M. A. Ali Shaikh and M. S. Bashar, Effect of argon pressure on the physical characteristics of cadmium telluride (CdTe) thin films by close-spaced sublimation, *J. Mater. Sci.: Mater. Electron.*, 2023, **34**, 344.

54 V. Dimitrov and S. Sakka, Linear and nonlinear optical properties of simple oxides. II, *J. Appl. Phys.*, 1996, **79**, 1741.

55 S. K. Tripathy, Refractive indices of semiconductors from energy gaps, *Opt. Mater.*, 2015, **46**, 240–246.

56 T. S. Moss, A relationship between the refractive index and the infra-red threshold of sensitivity for photoconductors, *Proc. Phys. Soc*, 1950, **63**, 167–176.

57 N. M. Ravindra, S. Auluck and V. K. Srivastava, On the Penn gap in semiconductors, *Phys. Status Solidi B*, 1979, **93**, 155–160.

58 P. Herve and L. K. J. Vandamme, General relation between refractive index and energy gap in semiconductors, *Infrared Phys. Technol.*, 1994, **35**, 609–615.

59 I. C. Nworie, S. M. U. Ishiwu, P. E. Agbo, A. O. Ojobeagu, P. B. Otah, C. Mbamara and B. Ojobo, Comparative assessment of optical and solid-state characteristics in antimony-doped chalcogenide thin films of ZnSe and PbSe to boost photovoltaic performance in solar cells, *Niger. J. Phys.*, 2024, **33**(1), 16–22.

60 E. Sharma, P. B. Barman and P. Sharma, Evaluation of optical linear and non-linear parameters of thermally deposited GeTeSeGa thin films in nir (1–2.6 mm) wavelength range from their transmission spectra, *Optik*, 2020, **219**, 165181.

61 K. Tanaka, in, *Optical Nonlinearity in Photonic Glasses*, Springer Handbooks, 2017, pp. 1.

62 H. Ticha and L. Tichy, Semiempirical relation between non-linear susceptibility (refractive index), linear refractive index and optical gap and its application to amorphous chalcogenides, *J. Optoelectron. Adv. Mater.*, 2002, **4**, 381–386.

63 E. R. Shaaban, M. Mohamed, M. N. Abd-el Salam, A. Y. Abdel-Latief, M. A. Abdel-Rahim and E. S. Yousef, Structural, linear and nonlinear optical properties of annealed $As_{47.5}Se_{47.5}Ag_5$ thin films for optoelectronic applications, *Opt. Mater.*, 2018, **86**, 318–325.

64 J. B. Dory, C. Castro-Chavarria, A. Verdy, J. B. Jager, M. Bernard, C. Sabbione, M. Tessaire, J. M. Fédéli, A. Coillet, B. Cluzel and P. Noé, Ge–Sb–S–Se–Te amorphous chalcogenide thin films towards onchip nonlinear photonic devices, *Sci. Rep.*, 2020, **10**, 11894.

65 P. C. Kumar, S. Das, S. Mohanty, J. Panda, S. Supriya, D. Alagarasan and R. Naik, Enhanced photoresponse in a Ag_2S/In_2Se_3 heterojunction-based visible light photodetector, *RSC Adv.*, 2025, **15**, 14518–14531.

66 M. Sulaman, Y. Song, S. Yang, M. Li, M. I. Saleem, P. V. Chandraseakar, Y. Jiang, Y. Tang and B. Zou, Ultra sensitive solution-processed broadband photodetectors based on vertical field-effect transistor, *Nanotechn*, 2020, **31**, 105203.

67 F. Wang, L. Li, W. Huang, L. Li, B. Jin, H. Li and T. Zhai, Submillimeter 2D Bi_2Se_3 flakes toward high-performance infrared photodetection at optical communication wavelength, *Adv. Funct. Mater.*, 2018, **28**(33), 1802707.

68 S. Supriya, P. C. Kumar, M. Pradhan and R. Naik, Hydrothermally synthesized Bi-doped CdTe nanoparticles with tunable optical and photoresponse properties for visible photodetectors, *ACS Appl. Mater. Interfaces*, 2024, **16**, 33806–33818.

69 Z. Q. Zheng, J. D. Yao and G. W. Yang, Growth of centimetre-scale high-quality In_2Se_3 films for transparent, flexible and high-performance photodetectors, *J. Mater. Chem. C*, 2016, **4**, 8094–8103.

70 G. Kresse and J. Furthmüller, Efficient iterative schemes for *ab initio* total-energy calculations using a plane-wave basis set, *Phys. Rev. B:Condens. Matter Mater. Phys.*, 1996, **54**, 11169.

71 G. Kresse and J. Furthmüller, Efficiency of ab-initio total energy calculations for metals and semiconductors using a plane-wave basis set, *Comput. Mater. Sci.*, 1996, **6**, 15.

72 K. Momma and F. Izumi, VESTA 3 for three-dimensional visualization of crystal, volumetric and morphology data, *J. Appl. Crystallogr.*, 2011, **44**, 1272.

73 J. P. Perdew, K. Burke and M. Ernzerhof, Generalized gradient approximation made simple, *Phys. Rev. Lett.*, 1996, **77**, 3865.